Journal of Solid State Chemistry **145,** 739–750 (1999)
Article ID jssc.1998.8298, available online at http://www.idealibrary.com on IDEAL®

Interdiffusion-Induced Phase Changes of $Co_{1-x}O$/Zirconia Composites

Kun-Tsai Lin and Pouyan Shen[1]

Institute of Materials Science and Engineering, National Sun Yat-sen University, Kaohsiung, Taiwan

Received November 17, 1998; received in revised form March 18, 1999; accepted March 23, 1999

$Co_{1-x}O$ powders mixed with pure zirconia (ZrO_2) or yttira (Y_2O_3) partially stabilized zirconia (Y-PSZ) were sintered and annealed at 1300°C for 300 h, and the $Co_{1-x}O$/Y-PSZ composite also at 1600°C for 1–100 h to investigate interdiffusion-induced phase changes. Analytical electron microscopic observations indicated the formation of (Zr, Y)-codoped Co_3O_4 spinel from intra- and intergranular $Co_{1-x}O$ particles for all the fired composites. The spinel formation above the equilibrium temperature 900°C for pure $Co_{1-x}O/Co_3O_4$ pair can be rationalized by the substitution of Zr^{4+} (< 2 mol%) and Y^{3+} (< 1 mol%) for Co^{2+} to generate a considerable number of charge- and volume-compensating defects and paracrystalline array of defect clusters in the $Co_{1-x}O$ lattice. The (111) faulting of (Zr, Y)-codoped Co_3O_4 implies the possible presence of Zinc blende-type defect clusters with cation vacancies assembled along oxygen close packed (111) plane of $Co_{1-x}O$. About 6 mol% Co^{2+} dissolution of Y-PSZ was found to stabilize the cubic-phase of zirconia upon cooling to room temperature. A relatively larger flux of Co^{2+} from $Co_{1-x}O$ into Y-PSZ than the opposite flux of Zr^{4+} and Y^{3+} causes a net vacancy flux, hence the formation of Kirkendall pores around the $Co_{1-x}O$ particles.

1. INTRODUCTION

Aliovalent dopant cations are know to cause defect clustering and phase changes of ionic crystals at high temperatures; 3*d* transition metal oxides having the rock salt structure (e.g., $Fe_{1-x}O$, $Co_{1-x}O$, and $Ni_{1-x}O$) and zirconia with fluorite type structure have been extensively studied in this regard (1). In the present research, the $Co_{1-x}O/ZrO_2$ composites (with or without Y_2O_3 stabilizer) prepared by sintering and then annealing were studied by analytical electron microscopy (AEM). We focussed on three points: first, defect clustering and ordering of cation-doped $Co_{1-x}O$; second, stabilization of cubic (c-) and tetragonal (t-) zirconia; and third, interdiffusion induced pores, as delineated in the following sections.

$Fe_{1-x}O$ having a considerable degree of nonstoichiometry ($x \leq 0.15$ (2)), was known to possess defect clusters of 4 : 1 type with four octahedral vacant sites surrounding one Fe^{3+}-filled tetrahedral interstitial site (3). When aged at high temperatures, the 4 : 1 clusters may assemble into larger units (e.g., 13 : 4, 16 : 5 and form a paracrystal (4, 5)) which order further into Fe_3O_4 spinel or other ordered phases: p'' and p''' (6, 7). In contrast to $Fe_{1-x}O$, $Ni_{1-x}O$ has a very small x (ca. 0.001 at 1500°C (8)) and the occurrence of defect clustering is uncertain, whether from the theoretical point of view (9, 10) or based on experimental results (11–15). There is, however, clearer experimental evidence of defect clustering in cation-doped $Ni_{1-x}O$. For example, Zr-doped or (Zr, Y) co-doped $Ni_{1-x}O$ was found by analytical electron microscopy (AEM) to transform to a paracrystal and then Ni_3O_4 spinel when annealed at 1300°C or 1600°C (16, 17). In the case of $Co_{1-x}O$ with a moderate x (ca. 0.01 (18)), spontaneous oxidation to form Co_3O_4 spinel was known to occur by cooling below 900°C (19). In this study we intend to prove that (Zr, Y)-codoped and Zr-doped $Co_{1-x}O$ can transform to a spinel superstructure above 900°C. In addition, the spinel is reported to have (111) faults, suggesting the presence of zinc blende-type defect clusters, as predicted for 3*d*-transition metal monoxides (20).

In the case of the stabilization of zirconia, divalent or trivalent cations (e.g., Mg^{2+}, Ca^{2+}, and Y^{3+}) which introduce charge-compensating oxygen vacancies were commonly added to a considerable amount to form the so-called cubic stabilized zirconia (CSZ) with the c- (cubic) structure of fluorite (21). A less amount of dopant was known to result in the formation of partially stabilized zirconia (PSZ) with fine t-precipitates in the c-ZrO_2 matrix and, hence, a beneficial toughness in terms of martensitic t- (tetragonal) to monoclinic (m-) transformation (21, 22). A second dopant is commonly introduced into PSZ used for thermal barrier coatings on metals for applications at high temperatures. The formation of a reaction oxide interlayer, and the interdiffusion-induced phase changes, in particular the martensitic t–m transformation of zirconia, are of great concern to the adherence and toughness of the coatings (23). It has been reported that Ni^{2+} and Al^{3+} stabilize, whereas Ti^{4+} destabilizes the c-ZrO_2 (10 mol% Y_2O_3) for the PSZ coating

[1] To whom correspondence should be addressed. Fax: 886-7-5254099.

0022-4596/99 $30.00

(24). We report further in this article that Y-PSZ reacts with $Co_{1-x}O$ to stabilize the c-fluorite cell of zirconia.

Finally, a net flux of vacancies between phases, due to an unequal opposite flux of atoms, was known to cause Kirkendall effect, which may cause the formation of pores near the interphase interface (25). This behavior has been commonly reported for the diffusion couples of metal alloys including those involving unequal boundary diffusion (26), but it has been less studied for ceramic materials invovling a complex defect chemistry. In this research we focussed also on the formation of Kirkendall pores close to the $Co_{1-x}O$/zirconia interface which somehow affected the formation of defect clusters and the ordered phase in $Co_{1-x}O$.

2. EXPERIMENTAL

Reagent grade $Co_{1-x}O$ (Cerac, 2 μm in size), Y-PSZ (Cerac, with 6 mol% Y_2O_3 and 2 μm in size), and ZrO_2 (Cerac, 3 μm in size) powders were used to prepare pure $Co_{1-x}O$ and powder mixture batches of $Co_{1-x}O$/Y-PSZ (1 : 4 molar ratio) and $Co_{1-x}O/ZrO_2$ (1 : 4 molar ratio). The powder batches were ball-milled in deionized water, oven dried at 100°C, and dry-pressed at 650 MPa to form pellets ca. 5 mm in diameter and 2 mm in thickness. The $Co_{1-x}O$/Y-PSZ pellets were fired at 1600°C for 1, 5, 10, 50, and 100 h in an open air furnace and cooled in the furnace with a cooling rate of 5°C/min. The $Co_{1-x}O$/Y-PSZ, $Co_{1-x}O/ZrO_2$, and pure $Co_{1-x}O$ pellets were also fired at 1300°C for 300 h and cooled under the same conditions as above in order to compare the effect of dopants on the phase change.

X-ray diffraction (XRD, Cu$K\alpha$, 35 kV, 25 mA at 0.05° and 2 s per step up to 2θ angle 105°) was used to identify the phases. The calculated lattice parameters from each d-spacing were plotted against $\cos^2\theta/\sin\theta$ and extrapolated to $\theta = 90°$ to obtain the precise lattice parameter a_0 (27). Scanning electron microscopy (SEM, JSM6400 at 20 kV) was used to study the distribution of $Co_{1-x}O$ particles in the sintered zirconia matrix. Thin sections of the samples were Ar-ion milled to electron transparency and studied by analytical electron microscopy (AEM, JEOL 3010) at 300 kV for taking bright field image (BFI), dark field image (DFI), lattice image, selected area diffraction (SAD) pattern, and point-count energy dispersive X-ray (EDX) analysis. The EDX analysis was performed using L shell counts for Zr and Y and K shell counts for Co, and the principle of ratio method without absorption correction (28). The error of composition measurement was estimated to be within $\pm 5\%$. The electron diffraction pattern of the c- and t-phase assemblages of Y-PSZ was indexed according to the distorted version of a c-fluorite cell as adopted previously (29).

3. RESULTS

3.1. SEM and XRD

All the fired composites contain inter- and intragranular $Co_{1-x}O$ particles in the zirconia matrix according to SEM observations. XRD indicated further that the zirconia was predominantly c-phase and m-phase for the $Co_{1-x}O$/Y-PSZ and $Co_{1-x}O/ZrO_2$ composites, respectively, although fine t-precipitates could still be identified in the PSZ matrix by electron diffraction. The c-phase has a significantly smaller cell volume ($a_0 = 0.5135$ nm) than that of the original Y-PSZ powders ($a_0 = 0.5170$ nm), indicating interdiffusion between $Co_{1-x}O$ and Y-PSZ has occurred. On the other hand the $Co_{1-x}O$ phase was consumed by evaporation and dissolution into zirconia and, hence, too low in content to have accurate X-ray lattice parameter determination for the fired composites. AEM showed, in addition, the composition, microstructure, and phase changes of $Co_{1-x}O$ and zirconia due to mutual solid solution, as described in the following section.

3.2. AEM

3.2.1. Defect Clusters and Ordered Structure of Monoxide

Electron diffraction indicated the formation of a $2 \times 2 \times 2$ superstructure, in fact (Zr, Y)-codoped Co_3O_4 spinel as indicated by latter EDX results, at the rim of $Co_{1-x}O$ particles for the $Co_{1-x}O$/Y-PSZ composite fired at 1600°C for 1 h (see Fig. 1 for a typical particle). In the sample fired at 1600°C for a longer period of time (50 h), the spinel phase was found to exhibit clear $\{111\}$ faults as shown representatively in Fig. 2. The submicron-sized $Co_{1-x}O$ particle in Fig. 2 has rotated into parallel epitaxial relationship with respect to the host Y-PSZ grain. In this regard, thermally activated Brownian rotation of intragranular particles toward epitaxial orientations was suggested to occur above a critical temperature for anchorage release, i.e., debonding of atoms, at the interface for a number of oxide composite systems: $Ni_{1-x}O$/Y-PSZ (30), $Ni_{1-x}O/NiAl_2O_4$ (31), and $Co_{1-x}O$/Y-PSZ (32). The lattice image from the same area as in Fig. 2 shows that the (111) fault is incommensurate, i.e., with varied spacing between faults, and the lattice planes are coherent across the $Co_{1-x}O$/spinel interface and the $Co_{1-x}O$/Y-PSZ interface (Fig. 3). It is noteworthy that the paracrystalline state and the spinel patches with (111) fault were both developed from the $Co_{1-x}O$ close to the $Co_{1-x}O$/Y-PSZ interface (Fig. 3). In fact, the paracrystal and the spinel phase can be identified by electron diffraction and lattice images from all samples. Figure 4 shows satellite diffraction spots of $Co_{1-x}O$ with a spacing ca. 1/2.8 times the lattice parameter in the reciprocal lattice. Thus, the paracrystalline distribution of defects is nearly 2.8 times the lattice spacing of the average structure of $Co_{1-x}O$ for

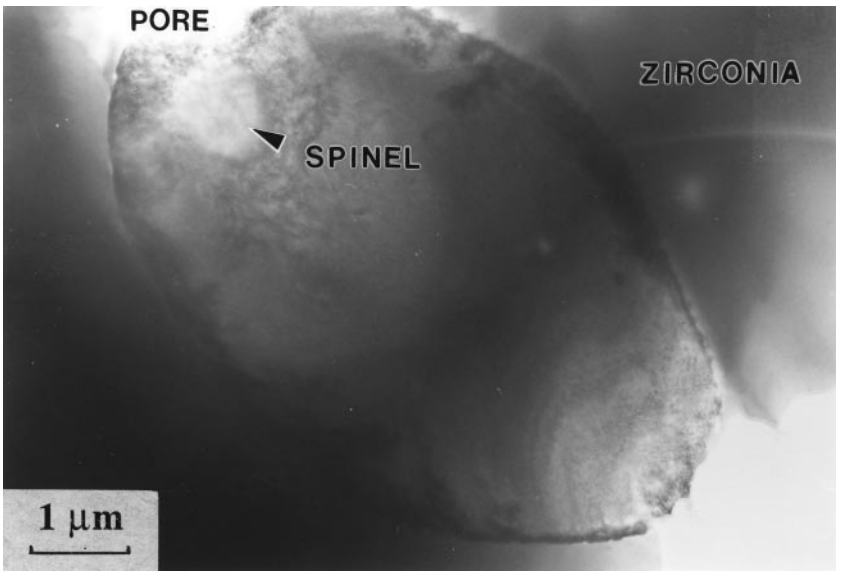

FIG. 1. TEM (BFI) of $Co_{1-x}O$/Y-PSZ composite fired at 1600°C for 1 h showing spinel phase was formed from $Co_{1-x}O$ near the pore.

(Zr, Y)-codoped $Co_{1-x}O$. Heterogeneous nucleation of the spinel phase, preferentially at the $Co_{1-x}O$/Y-PSZ interface and near the pore, was manifested also by intergranular $Co_{1-x}O$ particles (Fig. 5).

The cation-doped Co_3O_4 spinel phase was also formed in $Co_{1-x}O$/Y-PSZ and $Co_{1-x}O/ZrO_2$ composites when fired at a relatively low temperature (1300°C) for 300 h in air, as represented by the former case in Fig. 6. Under such a firing condition, the $Co_{1-x}O$ particles were always nonepitaxial with respect to the Y-PSZ grains. The pure $Co_{1-x}O$ pellet, which was subject to annealing at 1300°C for 300 h in air, also showed the spinel phase in its outer area, although in the form of fine precipitates (see Fig. 7a with inset [111] diffraction pattern). The pure Co_3O_4 spinel thus formed also has coherent lattice planes with respect to $Co_{1-x}O$ as indicated by lattice image taken along the [110] zone axis (Fig. 7b). It should be noted, however, that the inner area of the pellet is nearly devoid of the spinel phase (not shown).

3.2.2. Concentration Profiles and Resultant Pores at Interface

Point-count EDX results of Zr, Y, and Co across the $Co_{1-x}O$/Y-PSZ interface for a typical intragranular $Co_{1-x}O$ particle are shown in Fig. 8 for the composite fired at 1600°C for 100 h. Interdiffusion was manifested by inward diffusion of Zr (< 2 mol%), Y (< 1 mol%) and outward diffusion of Co (ca. 6 mol%) for the $Co_{1-x}O$ particle. It should be noted that the spinel phase at the rim of the $Co_{1-x}O$ particle gave the same EDX counts of Zr and Y as the $Co_{1-x}O$ particle. The composite fired at 1300°C for 300 h showed similar concentration profiles across the $Co_{1-x}O$/Y-PSZ interface, although the mutual solid solubility is somewhat lower than that at 1600°C. About the same amount of Zr was dissolved in the $Co_{1-x}O$ particle when reacted with ZrO_2 instead of Y-PSZ at 1300°C for 300 h, as shown by the concentration profiles in Fig. 9.

The $Co_{1-x}O$ particles in the $Co_{1-x}O$/Y-PSZ composite fired at 1600°C were more or less surrounded by pores (Fig. 10a) and with corrugated boundary (Fig. 10b), which can be ascribed to unequal flux of atoms across and along the $Co_{1-x}O$/Y-PSZ interface as discussed in Section 4.2.

3.2.3. Phase Change of Zirconia

Both c- and t-zirconia phases occurred in (Co, Y)-codoped zirconia, as indicated by electron diffraction of the $Co_{1-x}O$/Y-PSZ composite fired at 1600°C and then cooled to room temperature (Fig. 2). It is noteworthy that the Y-PSZ showed a t-precipitate free zone (PFZ) in the vicinity of $Co_{1-x}O$ particle, in sharp contrast to the rest area with (c + t)-tweed-texture contrast in BFI (Fig. 6). EXD analysis, however, could not resolve the composition difference between PFZ and the finely tweed-textured area. Diffuse electron diffraction (Fig. 6b) indicated that the c-zirconia phase must have a considerable number of oxygen vacancies to form defect clusters analogous to those reported for ZrO_2–Y_2O_3 solid solution (33).

The zirconia that dissolved with ca. 5–6 mol% Co in the $Co_{1-x}O/ZrO_2$ composite fired at 1300°C for 300 h was found to be m-phase when cooled to room temperature. The presence of mosaic twinning of the m-phase and the microcracks of the fired pellet indicated that a martensitic t–m transformation has occurred during cooling. In other

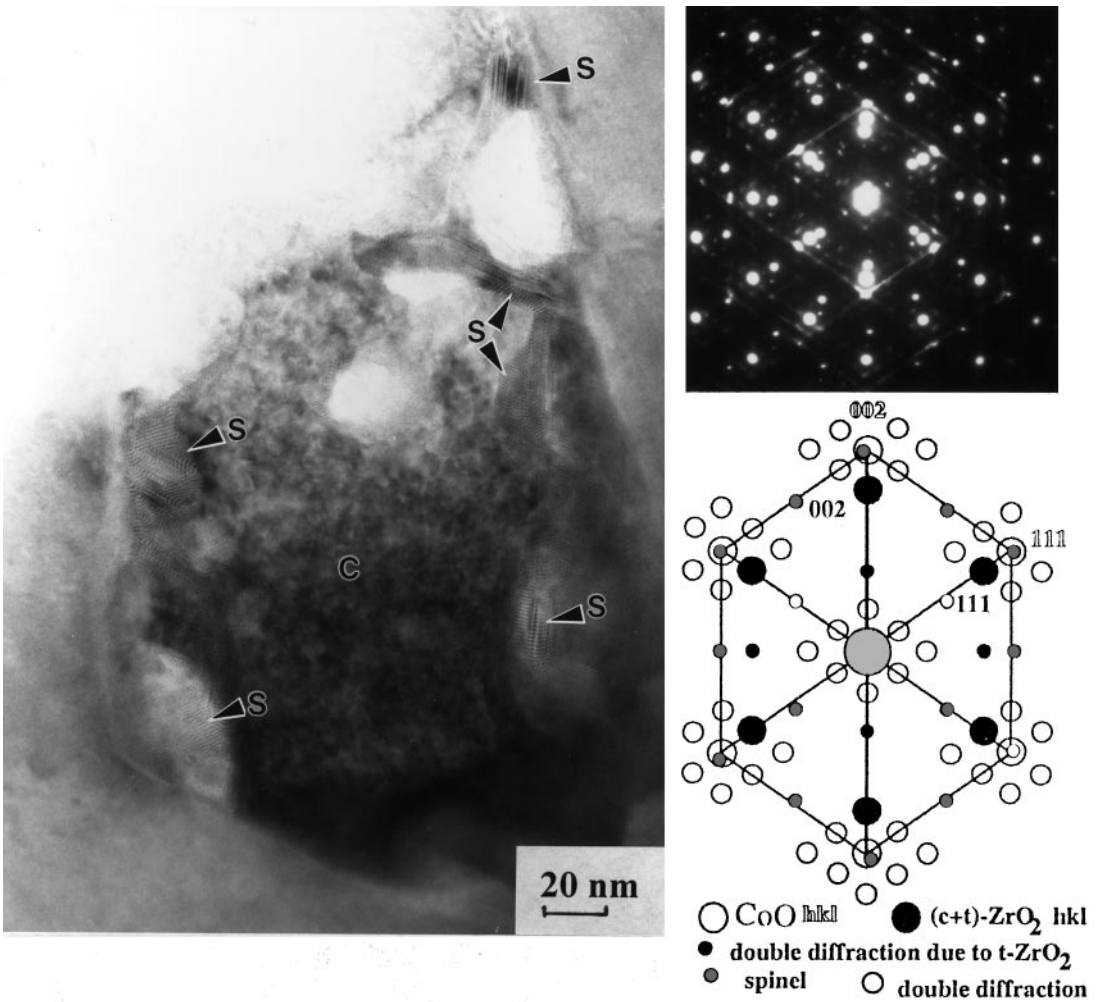

FIG. 2. TEM (BFI) with inset SAD pattern in [1$\bar{1}$0] zone axis of an intragranular $Co_{1-x}O$ (C) particle which has parallel-epitaxial orientation with respect to Y-PSZ and contains (111) faulted spinel (S) at the $Co_{1-x}O$/Y-PSZ interface, $Co_{1-x}O$/Y-PSZ composite fired at 1600°C for 50 h.

words, the t-phase is the stable phase for Co-doped zirconia at 1300°C as discussed further in Section 4.3.

4. DISCUSSION

4.1. Defect Chemistry of Cation-Doped $Co_{1-x}O$

(*a*) *Effect of* Co^{3+}

At temperatures below 900°C, $Co_{1-x}O$ oxidizes spontaneously to Co_3O_4 in the atmosphere (19). The generation of an electron hole or $Co_{Co}^{3+\cdot}$ in the $Co_{1-x}O$ lattice may proceed through the equations (34) in Kröger–Vink notation (35):

$$1/2O_2 \rightarrow V_{Co}^{x} + O_O^{x} \qquad [I]$$

$$V_{Co}^{x} \rightarrow V'_{Co} + h^{\bullet} \qquad [II]$$

$$V'_{Co} \rightarrow V''_{Co} + h^{\bullet}. \qquad [III]$$

In this notation, the type of imperfection is indicated by a major symbol, the location is described by a subscript, and finally the charge of the defect relative to the normal lattice is indicated by a superscript. Hence, O_o^x signifies a neutral charged oxygen atom in the normal lattice site; V_{Co}^{x}, V'_{Co}, and V''_{Co} represents a neutral, single, and double negatively charged cobalt vacancy, respectively; $h^{\bullet}$ signifies the electron hole. V'_{Co} is in fact V''_{Co} associated with an electron hole localized to form a bound pair of point defects on the octahedral Co sites, i.e., $[V''_{Co} + Co_{Co}^{3+\bullet}]$ analogous to the nature of "singly charged nickel vacancies" in $Ni_{1-x}O$ (36). Below 900°C, we suggest that Co^{3+} may also reside in the interstitial tetrahedral site (i.e., $Co_i^{\bullet\bullet}$) to form 4:1 clusters $[Co_i^{\bullet\bullet} + 4V''_{Co} + 4Co_{Co}^{\bullet}]$ and, hence, spinel phase with cations in both tetrahedral and octahedral sites. (A single 4:1 cluster has local topology similar to the spinel structure, but it is not sufficiently large to constitute a spinel phase.) In this regard, theoretical calculation indicated that interstitial

FIG. 3. Lattice image magnified from the $Co_{1-x}O$/Y-PSZ interface of Fig. 2, showing that the paracrystalline (P) state and (111) fault of spinel (S) were developed from the $Co_{1-x}O$ (C).

tetrahedral dopant can stabilize the 4 : 1 clusters and clusters of 4 : 1 clusters for 3*d* transition metal monoxides, e.g., Fe^{3+}-doped $Ni_{1-x}O$ and Mn^{3+}-doped $Co_{1-x}O$ (37).

The present observation indicated that the outer areas of the fired $Co_{1-x}O$ pellets were partially oxidized as the spinel phase whereas the interior of the sample was nearly immune from oxidation. This can be rationalized by a higher oxygen fugacity toward the sample surface, in accordance with a higher defect concentration near the $Co_{1-x}O$ surface (38). Alternatively, surface nucleation of the spinel phase is beneficial in minimizing strain and/or surface energies and can be facilitated by a higher diffusivity of cation vacancies at surface analogous to $Ni_{1-x}O$ (39). Nevertheless, the degree of nonstoichiometry must be sufficiently large in order to form defect clusters and the spinel phase from rock salt type monoxides, because $Ni_{1-x}O$ with a much smaller x than $Co_{1-x}O$ failed to form Ni_3O_4 spinel upon cooling from high temperature (17).

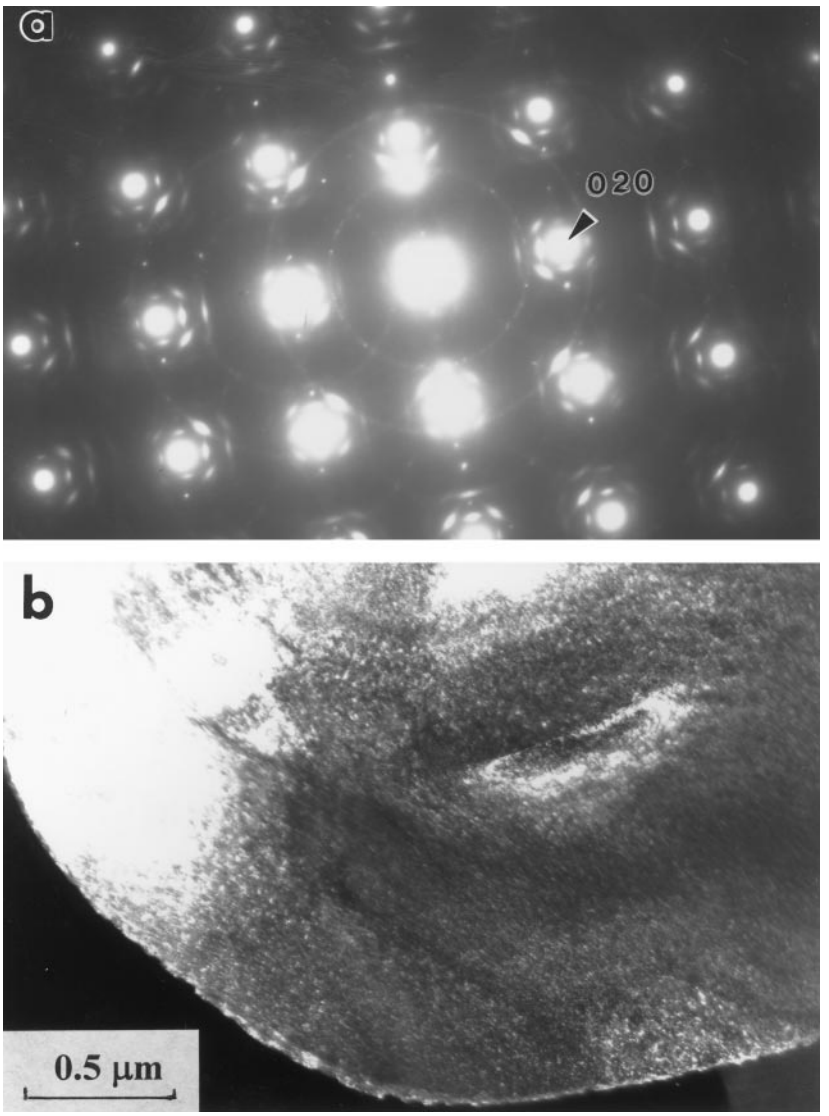

FIG. 4. (a) [001] SAD pattern showing fundamental and satellite spots of $Co_{1-x}O$. (b) DFI with $g = 220$, $Co_{1-x}O$/Y-PSZ composite fired at 1600°C for 100 h.

(b) Effect of Zr^{4+}, Y^{3+}, and Oxygen Flux

In oxides of the fluorite type, Zr^{4+} and Y^{3+} prefer to have seven- and eight-fold coordination, respectively (40). Thus it is conceivable that Zr^{4+} and Y^{3+} reside in octahedral substitutional sites, instead of interstitial tetrahedral sites for the $Co_{1-x}O$ lattice. The dopants are expected to cause charge-compensating defect clusters $[V''_{Co} + Co^{\bullet}_{Co}]$ through the equation (dominant $Zr^{\bullet\bullet}_{Co}$ as a representative):

$$ZrO_2 \xrightarrow{CoO} Zr^{\bullet\bullet}_{Co} + 2[V''_{Co} + Co^{\bullet}_{Co}] + 2O^{x}_{O}. \qquad [IV]$$

Here $Zr^{\bullet\bullet}_{Co}$ signifies a double positively charged zirconium at cobalt sites in the crystal lattice. It is also possible that the volume-compensating effect due to the substitution of Co^{2+} (effective ionic radii, 0.065 and 0.0745 nm for low spin and high spin, respectively) with Zr^{4+} (0.072 nm) and much larger Y^{3+} (0.090 nm) in coordination number (CN) 6 (41) forced $Co^{3+\bullet}_{Co}$ to enter the interstitial tetrahedral site, i.e., $Co^{\bullet\bullet\bullet}_{i}$, and, hence, more charge-compensating cation vacancies through the equation (dominant $Zr^{\bullet\bullet}_{Co}$ as a representative):

$$Zr^{\bullet\bullet}_{Co} + [V''_{Co} + Co^{\bullet}_{Co}] \rightarrow Zr^{\bullet\bullet}_{Co} + [Co^{\bullet\bullet\bullet}_{i} + 4V''_{Co} + 4Co^{\bullet}_{Co}]. \qquad [V]$$

Thus, above 900°C the equilibrium temperature for undoped $Co_{1-x}O/Co_3O_4$ pair in atmosphere, the 4:1 type

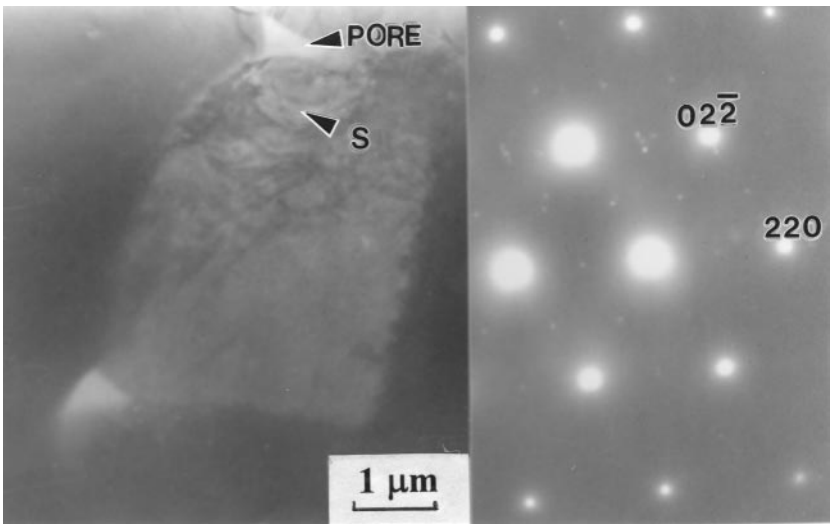

FIG. 5. TEM (BFI) and inset SAD pattern ($Z = [\bar{1}11]$) of an intergranular $Co_{1-x}O$ particle with spinel superstructure nucleated near a pore, $Co_{1-x}O$/Y-PSZ composite fired at 1600°C for 100 h.

defect clusters, the paracrystalline ordered state, and then spinel can be activated through reaction [V].

Oxygen vacancies can also be introduced around $Zr_{Co}^{\cdot\cdot\cdot\cdot}$ and $Y_{Co}^{\cdot}$ for volume compensation and, hence, affect the defect structure and the migration mechanisms of the surrounding $Co_{1-x}O$. A higher oxygen mobility is thus expected for the $Co_{1-x}O$ lattice around the dopants. In fact, microanalysis of an oxidized CoO-zirconia (CaO stabilized)

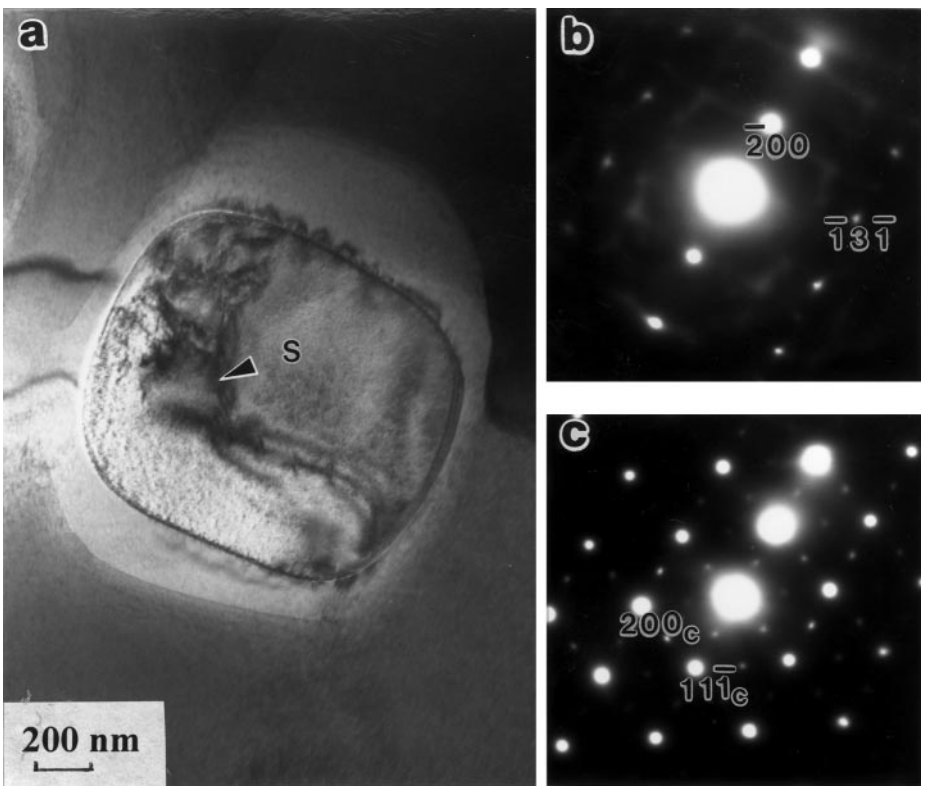

FIG. 6. TEM (BFI) of $Co_{1-x}O$/Y-PSZ composite fired at 1300°C for 300 h showing intragranular $Co_{1-x}O$ particle contianing spinel (S) phase, but no epitaxial crystallograhpic relationship between Y-PSZ host and $Co_{1-x}O$ with their SAD patterns in (b) $Z = [013]$ and (c) $Z = [011]$, respectively.

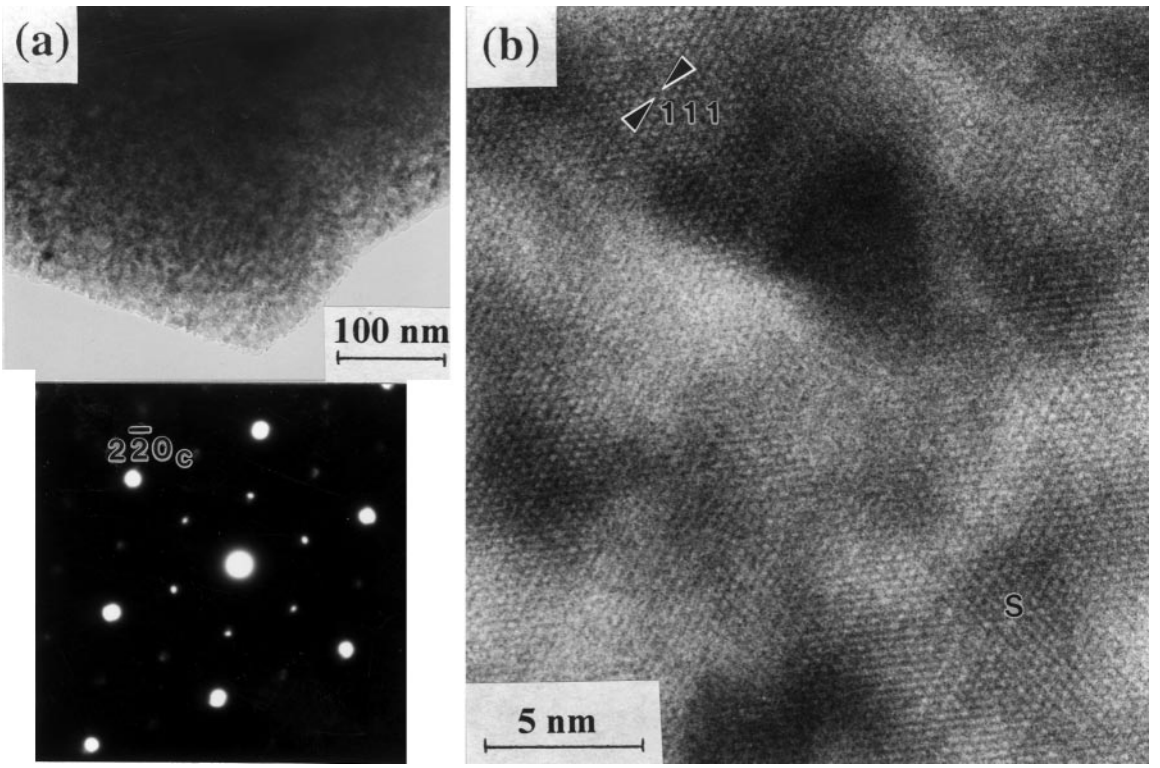

FIG. 7. (a) TEM (BFI) and inset SAD pattern ($Z = [111]$) of the outer area of the $Co_{1-x}O$ pellet subject to postsintering annealing at 1300°C for 300 h, showing fine precipitates of spinel phase (b) lattice image taken from (a) but tilted to $[1\bar{1}0]$ zone axis.

eutectic (42) and parallel-detection electron energy-loss (PEEL) spectometer analysis of $Co_{1-x}O$ coating on zirconia (CaO steabilized) (43) indicated a higher oxygen concentration for $Co_{1-x}O$ toward the interface, due to a relatively higher diffusivity of oxygen in zirconia than in $Co_{1-x}O$. The abrupt change of oxygen concentration thus may account for the formation of Co_3O_4 spinel at the interface of diffusion couples, including that at the scale of individual grains as in the present case. On the other hand, $Co_{1-x}O$ coating overlaid on zirconia powders via the sol–gel route remained as rock salt structure (44). It is not certain whether the negligible oxidation of $Co_{1-x}O$ in such a case is due to the reducing role of carbon in the precursor phase or simply the size dependence of phase stability.

(c) Cause and Implication of (111) Faulting of Spinel

The (Zr, Y)-codoped Co_3O_4 showed (111) faulting, in sharp contrast with that derived from pure $Co_{1-x}O$ by oxidation or prepared by hot pressing (800°C/30 MPa) and hot isostatic pressing (880°C/196 MPa) (45). In this connection, it is of interest to note that an applied stress as high as 11–17 kbar was required to trigger (111) faulting for a germante spinel (Mg_2GeO_4) at temperatures around 1000°C (46). Apparently in the present case, it was the dissolution of Zr^{4+} and Y^{3+}, rather than the lower internal stress due to sintering, that caused the faulting of the Co_3O_4 spinel.

The Co_3O_4 spinel was known to be nonstoichiometric (i.e., $Co_{3-x}O_4$ in formula) having Co vacancies increasing in number with the decrease of temperature (47). The dissolution of Zr^{4+} and Y^{3+} in the $Co_{3-x}O_4$ spinel is expected to increase the number of Co vacancies analogous to the case of (Zr, Y)-codoped $Co_{1-x}O$. The (111) faulting of (Zr, Y)-codoped $Co_{3-x}O_4$ may be a result of specific arrangement of Co vacancies within the spinel framework and its monoxide precursor. Our tentative explanation is that the (111) faulting implies the presence of zinc blende type defect clusters (e.g., 16:7 derived from 4:1 clusters by corner sharing (20)) in (Zr, Y)-codoped $Co_{1-x}O$, because such types of cluster have cation vacancies assembled along oxygen close-packed (111) planes which is beneficial for crystallograhpic shear to cause intersecting faults on several different $\{111\}$ planes, as shown by the spinel patches with two sets of $\{111\}$ faulting edge-on (in the $[1\bar{1}0]$ zone axis) in Fig. 2. Nevertheless, future two-beam dark-field electron microscopy is required to determine the exact nature, e.g., stacking vector of the fault. It should be noted that the paracrystalline ordered state (5) and the spinel phase (6, 7) can be derived from corner-shared 4:1 clusters such as 13:4 and/or 16:5 defect clusters for the analogue oxide, i.e.,

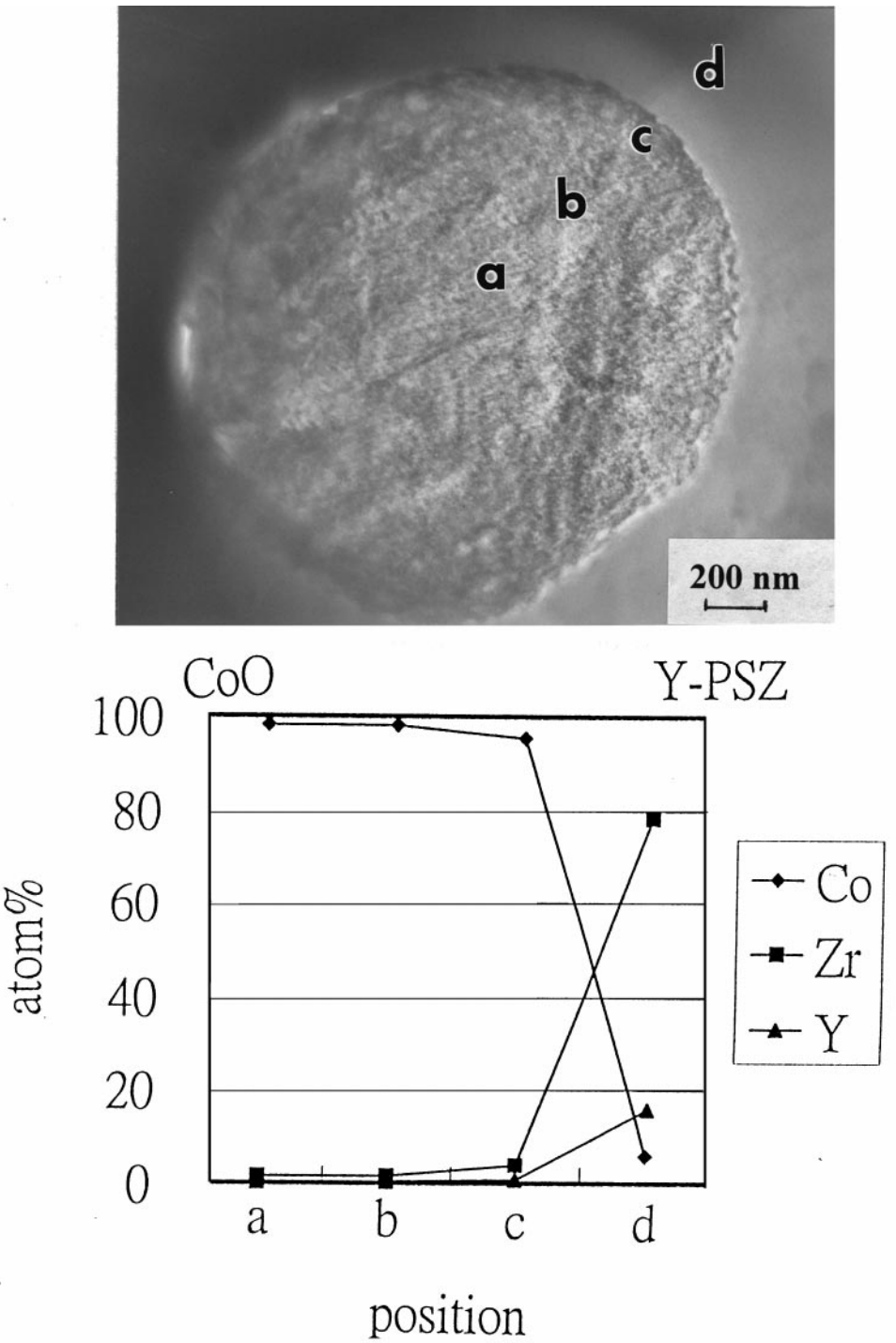

FIG. 8. TEM (BFI) and point-count EDX concentration profiles (a to d) across the $Co_{1-x}O$/Y-PSZ interface for intragranular $Co_{1-x}O$ particle, $Co_{1-x}O$/Y-PSZ composite fired at 1600°C for 100 h.

$Fe_{1-x}O$ (5). The (111) faulting of the present spinel however implies that zinc blende type defect clusters are also present for (Zr, Y)-codoped $Co_{1-x}O$. It remains to be clarified whether or not the dopant type and level affect the assembly mechanisms of the 4:1 clusters for $Co_{1-x}O$ and other transition metal monoxides.

4.2. Kirkendall Pores and Diffusion-Induced Grain-Boundary Migration

The open space between compact powders could survive a sintering event as inter- and intragranular pores. However, the pores that clustered at the rim of the intragranular

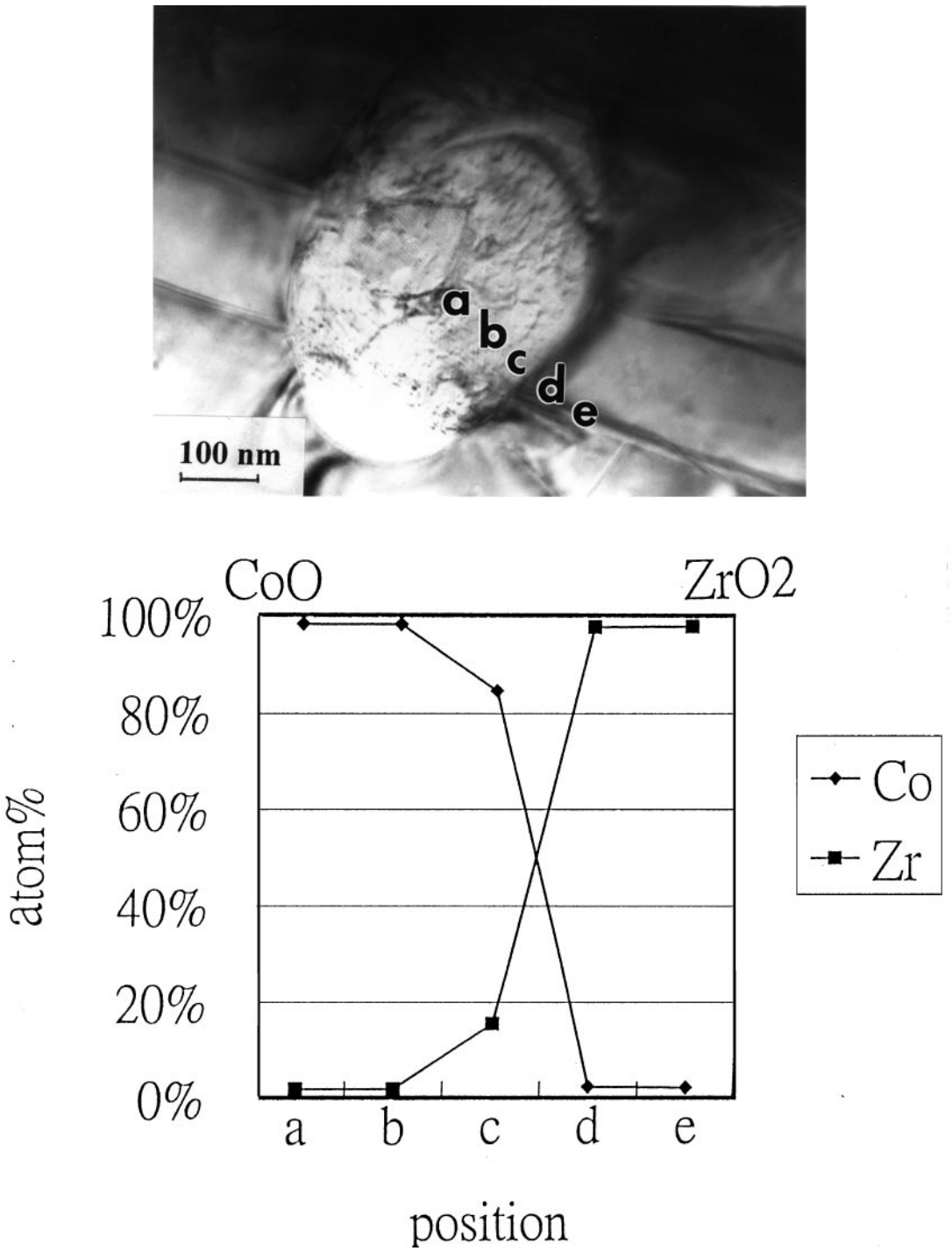

FIG. 9. TEM (BFI) and point-count EDX concentration profiles (a to e) across the $Co_{1-x}O/ZrO_2$ inteface for intragranular $Co_{1-x}O$ particle in the $Co_{1-x}O/ZrO_2$ composite fired at 1300°C for 300 h.

$Co_{1-x}O$ particles cannot be regarded simply as residue of a densification process. Instead, we suggest that a relatively larger flux of Co^{2+} (ca. 6 mol%) from $Co_{1-x}O$ into Y-PSZ compared to the reverse flux of Zr^{4+} (< 2 mol%) and Y^{3+} (< 1 mol%) caused a net vacancy flux, hence the formation of Kirkendall pores around the $Co_{1-x}O$ particles. The net number of vacancies near the interface must vary with time in the early stage of interdiffusion. This kinetic factor may

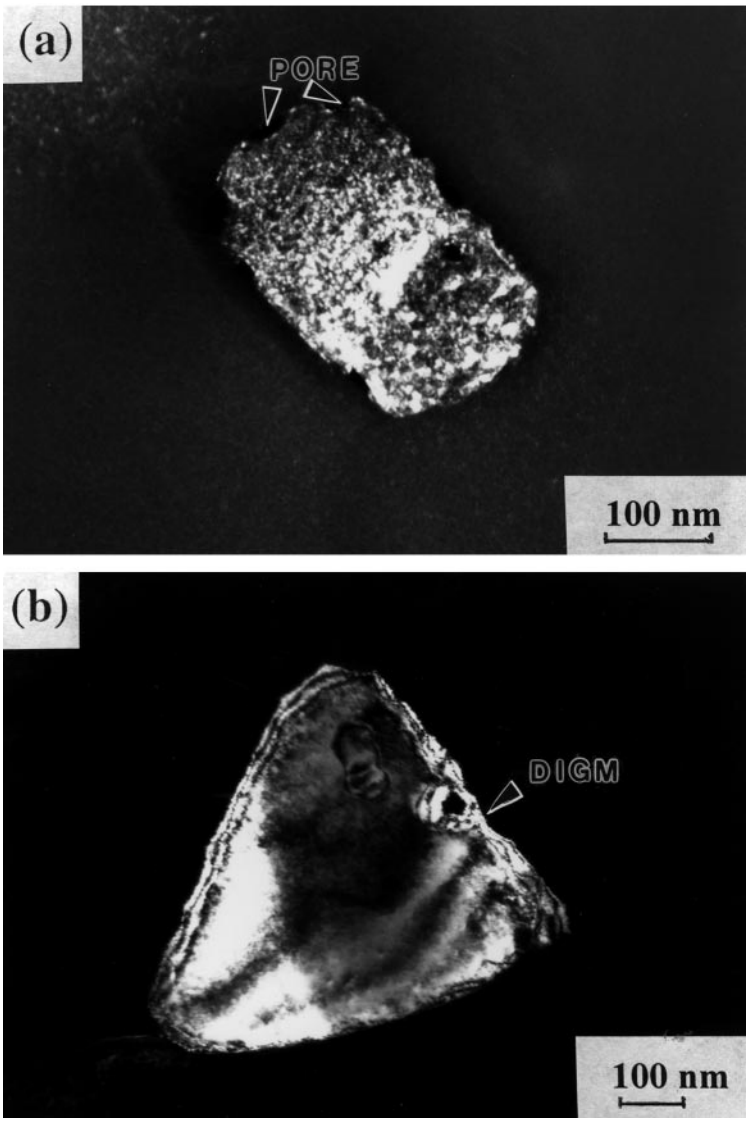

FIG. 10. TEM (DFI) of (a) intragranular $Co_{1-x}O$ particle ($g = 220$) surrounded by Kirkendall pores, $Co_{1-x}O$/Y-PSZ composite fired at 1600°C for 100 h; (b) Intergranular $Co_{1-x}O$ particle with corrugated grain boundary indicating DIGM, $Co_{1-x}O$/Y-PSZ composite fired at 1600°C for 10 h.

account for the varied extent of Kirkendall pore formation among the samples. By contrast to the $Co_{1-x}O$/Y-PSZ pair, the mutual solid solubilites of $Ni_{1-x}O$ and Y-PSZ are nearly equal (ca. 2 mol%) at 1600°C (17): hence, there is a shortage of net vacancies for the Kirkendall pore formation at the $Ni_{1-x}O$/Y-PSZ interface.

It should be noted that the corrugated interface, a general indicator of diffusion-induced grain-boundary migration (DIGM, a grain boundary analogue of Kirkendall effect (26)) was observed for intergranular $Co_{1-x}O$ particles even though the composite was fired at a rather high temperature. It is likely that grain boundary diffusion was more significant for inter- than intragranular $Co_{1-x}O$ particles even at a temperature as high as 1600°C.

4.3. Effect of Cation Dopant on the Stabilization of Zirconia

Interdiffusion between the $Co_{1-x}O$ particle and the Y-PSZ caused the formation of (Co, Y)-PSZ and a PFZ next to the $Co_{1-x}O$ particle. Both the PFZ and the finely tweed textured (Co, Y)-PSZ have a higher content of Co^{2+} and Y^{3+} (ca. 6 and 14 at%, respectively) than the original Y-PSZ powders, indicating that the co-dissolution of Co^{2+} and Y^{3+} stabilized the c-fluorite cell of zirconia considerably. The cation dopants presumbaly substitute for Zr^{4+} to generate charge-compensating oxygen vacancies, the key stabilizer of the c-fluorite structure (21). In this connection, it is interesting to note the recent X-ray absorption study using synchrotron radiation (40), which indicated that

oversized dopant Y^{3+} is eight-fold coordinated with nearby Zr^{4+} in seven-fold coordination (i.e., an oxygen vacnacy prefers to be associated with Zr^{4+}). On the other hand, an undersized dopant such as Fe was forced to compete with Zr ions for the oxygen vacancies in zirconia resulting in sixfold oxygen coordination for the dopant and a large disturbance to the surrounding next neareset neighbors (48). The dopant Co^{2+}, being undersized with respect to Zr^{4+}, must create oxygen vacancies nearby; hence, it is an effective stabilizer for the c-fluorite cell.

The solid solubility of Co^{2+} in pure zirconia is too low (only one third as much as that in Y-PSZ to stabilize the c-fluorite cell at 1300°C. Instead, the zirconia was found to be m-phase with characteristic multiple transformation twinning at room temperature, indicating that the t-phase was the stable phase before cooling. The martensitic transformation temperature for Co^{2+}-dissolved zirconia is expected to be lower than that for pure zirconia due to the effect of Co^{2+} dopant on the stabilization of the t-phase, as indicated by the t/m univariant for analogue PSZ (21). The present Co^{2+}-doped t-zirconia presumbaly exceeds the critical size for martensitic transformation (21), hence became m-phase upon cooling from 1300°C to room temperature.

5. SUMMARY

1. At 1600°C and 1300°C, (Zr, Y) co-doping or Zr-doping activate defect clustering and ordering of the $Co_{1-x}O$ lattice to form a paracrystalline ordered state and a spinel superstructure. The $Co_{1-x}O$/zirconia interface and pores around the $Co_{1-x}O$ particles were preferred nucleation sites of the defect clusters and the spinel phase.

2. The inward diffusion of Zr^{4+}, Y^{3+}, O^{2-}, and outward diffusion of Co^{2+} for $Co_{1-x}O$ particles caused the formation of Kirkendall pores around the particles.

3. The (Zr, Y)-codoped Co_3O_4 showed (111) faulting, presumably due to defect clusters of the zinc blende-type with cation vacancies assembled along the oxygen closed-packed (111) plane, making it feasible for crystallographic shear to occur.

4. Dissolution of Co^{2+} in Y-PSZ caused the stabilization of the c-fluorite cell of zirconia.

REFERENCES

1. P. Kofstad, "Nonstoichiometry, Diffusion, and Electrical Conductivity in Binary Metal Oxides." Wiley Interscience, New York, 1972.
2. B. E. F. Fender and F. D. Riley, "The Chemistry of Extended Defects in Non-Metallic Solids" (L. Eyring and M. O'Keefe, Eds.). North-Holland, Amsterdam, 1970.
3. C. R. A. Catlow and B. E. F. Fender, *J. Phys. C*: *Solid State Phys.* **8,** 3267 (1975).
4. T. R. Welberry and A. G. Christy, *J. Solid State Chem.* **117,** 398 (1995).
5. T. R. Welberry and A. G. Christy, *Phys. Chem. Minerals* **24,** 24 (1997).
6. P. Vallet and P. Raccah, *Mem. Sci. Rev. Metall.* **62,** 1 (1965).
7. B. Andersson and J. O. Sletnes, *Acta Crystallogr. Sect. A* **33,** 268 (1977).
8. H. G. Sockel and H. Schmalzried, *Ber. Bunsenges. Phys. Chem.* **72,** 745 (1968).
9. C. R. A. Catlow and A. M. Stoneham, *J. Am. Ceram. Soc.* **64,** 234 (1981).
10. R. W. Grime, A. B. Anderson, and A. H. Heuer, *J. Am. Ceram. Soc.* **69,** 619 (1986).
11. W. C. Tripp and N. M. Tallan, *J. Am. Ceram. Soc.* **53,** 531 (1970).
12. M. L. Volpe and J. Reddy, *J. Chem. Phys.* **53,** 1117 (1970).
13. C. M. Osburn and R. W. Vest, *J. Phys. Chem. Solids* **32,** 1331 (1971).
14. R. L. Lalauze and J. H. Meunier, *Oxid. Met.* **12,** 183 (1978).
15. J. Szuber, *J. Mater. Sci.* **19,** 1991 (1984).
16. P. Shen, S. Chen, and H. S. Liu, *Mater. Sci. Eng. A* **161,** 135 (1993).
17. J. Chen and P. Shen, *J. Solid State Chem.* **140,** 361–370 (1998).
18. S. M. Tomlinson, C. R. A. Catlow, and J. H. Harding, *J. Phys. Chem. Solids* **51,** 477 (1990).
19. M. Oku and Y. Sato, *Appl. Surf. Sci.* **55,** 37 (1992).
20. A. B. Anderson, R. W. Grimes, and A. H. Heuer, *J. Solid State Chem.* **55,** 353 (1984).
21. D. J. Green, R. H. J. Hannink, and M. V. Swain, "Transformation Toughening of Ceramics." CRC Press, Boca Raton, FL, 1989. [and references cited therein].
22. D. L. Porter and A. H. Heuer, *J. Am. Ceram. Soc.* **60,** 183 (1977).
23. S. Chen, Ph.D. thesis, National Sun Yat-sen University, Taiwan, 1990.
24. S. Chen, W. Deng, and P. Shen, *Mater. Sci. Eng. B* **22,** 247 (1994).
25. M. Watanabe, Z. Horita, D. J. Smith, M. R. McCartney, T. Sano, and M. Nemoto, *Acta Metall. Mater.* **42,** 3381 (1994).
26. R. W. Balluffi and J. W. Cahn, *Acta Metall.* **29,** 493 (1981).
27. B. D. Cullity, 'Elements of X-Ray Diffraction." Addison–Wesley, Reading, MA, 1978.
28. D. B. Williams, "Practical Analytical Electron Microscopy in Materials Sciences," p. 157. Philips Electronic Instruments, Inc., Electron Optics, Mahwah, NJ, 1984.
29. G. Teufer, *Acta Crystal.* **15,** 1187 (1962).
30. J. Chen and P. Shen, *Scripta Metall.* **37,** 1287 (1997).
31. S. R. Wang and P. Shen, *Mater. Sci. Eng. A* **251,** 106 (1998).
32. K. T. Lin, M.S. thesis, National Sun Yat-sen University, Taiwan, 1998.
33. W. C. Mackrodt and P. M. Woodrow, *J. Am. Ceram. Soc.* **69,** 277 (1986).
34. K. Persels Constant, T. O. Mason, and J. L. Routbort, *J. Phys. Chem. Solids* **53,** 413 (1992).
35. F. A. Kröger and H. J. Vink, *Solid State Phys.* **3,** 307 (1956).
36. A. Atkinson, A. E. Hughes, and A. Hammou, *Phil. Mag. A* **43,** 1071 (1981).
37. R. W. Grime, A. B. Anderson, and A. H. Heuer, *J. Phys. Chem. Solids* **48,** 45 (1987).
38. J. Nowothy and I. Sikora, *J. Am. Ceram. Soc.* **65,** 192 (1982).
39. A. Atkinson and R. I. Taylor, *Phil. Mag. A* **43,** 979 (1981).
40. P. Li, I. W. Chen, and J. E. Penner-Hahn, *Phys. Rev. B* **48,** 10074 (1993).
41. R. D. Shannon. *Acta Crystallogr. Sect. A* **32,** 751 (1976).
42. J. Bentley, S. McKernan, C. B. Carter, and A. Revoolevschi, Inst. Phys. Conf. Ser. No. 138: Section 2, "Electron Microscopy and Analysis," p. 39, JOP, Bristol, UK, 1993.
43. H. I. Yoo and J. H. Lee, *J. Phys. Chem. Solids* **57,** 65 (1996).
44. H. C. Zeng, J. Lin, and K. L. Tan, *J. Mater. Res.* **10,** 3096 (1995).
45. S. Sakamoto, M. Yoshinaka, K. Hirota, and Y. Yamaguchi, *J. Am. Ceream. Soc.* **80,** 267 (1997).
46. P. C. Burnley and H. W. Green II, *Nature* **338,** 753 (1989).
47. S. Angelov, E. Zhecheva, R. Stoyanova, and M. Atanasov, *J. Phys. Chem. Solid* **51,** 1157 (1990).
48. P. Li, I. W. Chen, and J. E. Penner-Hahn, *J. Am. Ceram. Soc.* **77,** 118 (1994).